Structural vibration absorption in multilayered sandwich structures using negative stiffness nonlinear oscillators

PLEASE CITE THE PUBLISHED VERSION

https://doi.org/10.1016/j.apacoust.2021.108240

PUBLISHER

Elsevier

VERSION

AM (Accepted Manuscript)

PUBLISHER STATEMENT

This paper was accepted for publication in the journal Applied Acoustics and the definitive published version is available at https://doi.org/10.1016/j.apacoust.2021.108240.

Structural vibration absorption in multilayered sandwich structures using negative stiffness nonlinear oscillators

Han Meng[a], Xiuchang Huang[b], Yanyu Chen[c], Stephanos Theodossiades[d], Dimitrios Chronopoulos[e,f]

[a] *Department of Mechanical and Construction Engineering, Northumbria University, NE1 8ST, UK*
[b] *State Key Laboratory of Mechanical System and Vibration, Laboratory of Vibration, Shock & Noise, Shanghai Jiao Tong University, China*
[c] *Department of Mechanical Engineering, University of Louisville, Louisville, KY 40208, USA*
[d] *Wolfson School of Mechanical, Electrical and Manufacturing Engineering, Loughborough University, LE11 3TU, UK*
[e] *Institute for Aerospace Technology & The Composites Group, The University of Nottingham, NG7 2RD, UK*
[f] *Department of Mechanical Engineering & Division of Mechatronic System Dynamics (LMSD), KU Leuven, Ghent Technology Campus, 9000, Belgium*

Abstract

We hereby report on the incorporation of negative stiffness oscillators realized through Euler buckled beams within vibrating multilayered sandwich structures. Such devices have been extensively investigated as single degree of freedom isolation mechanisms when mechanical grounding is available. It is worth exploring the influences of implementing such mechanisms within continuous multilayered vibrating structures given their interesting nonlinear vibration isolation characteristics. A numerical investigation is presented in this work with the computed performance being compared against the one of linear oscillators of equal mass and damping properties. Despite the fact that the negative stiffness nonlinear (NSN) oscillators were not properly optimized for the specific application due to the implied computational cost, they exhibited superior performance to their linear counterparts in a broadband sense. Considering the dependence of the linear resonators' performance to manufacturing precision and narrowband excitation, the NSN concept is an excellent candidate for attenuating structural vibration across a wide spectrum.

Keywords: Nonlinear resonators, Vibration absorption, Mechanical metamaterials, Negative stiffness, Multilayered sandwich structure

---

1. Introduction

Installing oscillators in vibrating structures is an effective method to improve their vibration absorption capacity. The popular vibrational metamaterials are essentially structures

Email addresses: menghan1989.123@gmail.com (Han Meng), xchhuang@sjtu.edu.cn (Xiuchang Huang), yanyu.chen@louisville.edu (Yanyu Chen), S.Theodossiades@lboro.ac.uk (Stephanos Theodossiades), Dimitrios.Chronopoulos@nottingham.ac.uk (Dimitrios Chronopoulos)

consisting of host components and periodically/nonperiodically attached oscillators. For instance, Liu et al. [1] first fabricated crystals with periodically distributed oscillators made of hard cores and soft rubber coatings. Zhang et al. [2], Huang et al. [3], Langfeldt et al. [4], Chen et al. [5] and Peng and Pai [6] developed metamaterial beams, plates and sandwich structures with membrane or mass spring oscillators. Meng et al. [7–10] studied metamaterial beams with spatially varying cantilever-mass oscillators. Barnhart et al. [11], Peng et al. [12], Pai et al. [13], Xiao et al. [14] investigated metamaterials with multiple resonators with the purpose of broadening vibration absorption band. Xiao et al. [15] created metamaterial rods with coaxial rubber rings and metal rings oscillators. Li et al. [16] investigated the vibration suppression performances of metamaterial structures constituted of double sides stepped oscillators deposited on plates. Most of the existing metamaterials contain linear oscillators. The vibration energy can be greatly absorbed by the resonance of linear oscillators, the stop bands of metamaterials hence occur at the vicinity of the resonance frequencies of the linear oscillators. Broadband vibration absorption is hard to achieve by metamaterials with linear oscillators. Besides, the resonant frequencies of linear oscillators are proportional to their stiffness and reversely proportional to their mass. The mass of oscillators is generally restricted in applications to avoid adding extra burden to vibrating structures, the stiffness of oscillator therefore needs to be minimized to realize low frequency vibration absorption.

Negative stiffness mechanisms (NSMs) are structures that can exhibit a reversal of usual displacement to force ratio in some region. NSMs have been realized by different configurations. For instance, Carrella et al. [17, 18], Kovacic et al. [19], Tang and Brennan [20], Liu et al. [21] and Hao and Cao [22] proposed NSMs created with two oblique or horizontal springs connected at one end. These NSMs were connected with vertical springs to form the so called quasi-zero-stiffness structures. Yao et al. [23], Zhou et al. [24] and Wang et al. [25] developed vibration isolation platforms with cam-roller-spring mechanisms. Zhang and Zhao. [26], Sun and Jing [27], and Sun et al. [28] investigated nonlinear vibration isolation obtained by scissor like structures.Wu et al. [29], Dai et al. [30] and Bian and Jing [31] developed nonlinear vibration isolation systems with bio-inspired structures. Rigid bars were also used for the construction of NSMs. Platus [32], Yang et al. [33] and Wang et al. [34] studied the dynamic and power flow behaviors [21] of NSMs consisting of rigid bars hinged at the center with the other ends moving freely in horizontal guideway. Zhang et al. [35] and Le and Ahn [36] designed vibration isolation systems with rigid bar NSMs for high precision instruments and vehicle seat applications. Besides, bistable structures such as buckled beams were widely applied in the NSMs. Fulcher et al. [37], Kashdan et al. [38], Haberman [39] investigated the load-deformation response of buckled beams which displayed negative stiffness behaviors in the transition between two stable states. Virgin and Davis [40], and Lee et al. [41] used the buckled struts to design negative stiffness spring component for vibration isolation systems. Wooderd and Houserman [42] configured negative stiffness suspension system with two compressed beams. Liu et al. [43] and Huang et al. [44, 45] developed negative stiffness connectors formed by two compressed Euler beams hinged at both ends. Apart from the mechanical structures, magnetic and electromagnets were also adopted to construct NSMs. Xu et al. [46], Zheng et al. [47], and Wu et al. [48] proposed negative stiffness springs by virtue of the repulsive forces between a pair of fixed and freely sliding magnets, coaxial ring magnets and cuboidal magnets respectively. Robertson et al. [49] and Carrella et al. [50] and Dong et al. [51] investigated NSMs composed of a center floating magnet and two magnets at different sides which exerted attraction forces on the center magnet. These NSMs were combined with mechanical springs to form high-static–low-dynamic stiffness isolator. Tunable [52] electromagnet NSMs could be realized by replacing some magnet components with electromagnets. Zhou and Liu [53, 54] constructed an electromagnet NSM in which a center permanent magnet was placed between a pair of electromagnets. Pu et al. [55] proposed negative stiffness springs with coils and coaxial magnets. The stiffness of these NSMs was tuned by controlling the current.

The NSMs have found wide applications in vibration isolation systems. A popular application is the nonlinear energy sink, which is a local attachment with nonlinear typically cubic and negative stiffness that could effectively absorb vibration within a broader spectrum of frequency compared with linear attachments [56–59]. The NSMs were mostly implemented in vibration isolation systems that were connected to mechanical grounding, only a few studies were conducted regarding continuous vibrating structures with NSMs. Zhou et al. [60–62], Casalotti et al. [63] and Wang et al. [64, 65] proposed metamaterial beams, rods and plates that achieved low frequency band by using NSMs. Kani et al. [66] investigated the energy transfer from a simple supported continuous beam to the nonlinear energy sink. The seminal work presented in [64] is the first one to exhibit the advantages of incorporating NSMs within 2D continuous vibrating structures. The authors focused on extracting the band structure of the structural unit cell using a plane-wave expansion method and considering the linearized stiffness of the oscillators. We hereby expand the above analysis to NSMs comprising Euler buckled beams and also through employing finite element modelling to capture the full effects of nonlinearity on the structural response.

Multilayered sandwich structures are widely employed within the transport and energy industries thanks to their high stiffness over mass performance indices. Despite their advantages, the low mass and high stiffness of such structures implies high vibrational and acoustic transmissibility with low frequency vibration absorption being an important open technological issue. Inspired by the designing ideas of metamaterial structures and NSMs, we analyzed the structural responses of negative stiffness nonlinear (NSN) oscillators consisting of hinged buckled Euler beam NSMs and oscillating mass incorporated in a vibrating unit, and implemented for the first time the NSN oscillators in the cores of multilayered sandwich structures to improve their structural vibration absorption performance. The multilayered sandwich structures with NSN oscillators were modeled through a 3D finite element (FE) approach which can accurately estimate the structural responses in wide frequency ranges as well as in time domain. In addition, we compared the frequency responses between sandwich structures with NSN oscillators and linear resonators of the same mass while tuned for different frequency bands to give out a further insight of the influences of the NSN oscillators.

This paper is structured as follows: Section 2 presents the employed NSN oscillators, analyzes the structural responses of a vibrating unit with the NSN oscillator, and searches for designs that are able to perform interwell vibration. Section 3 investigates the vibration absorption performances of multilayered sandwich structures that incorporate the abovementioned NSN oscillators. Design optimization and necessary future developments of NSN structures are pointed out in Section 4. Concluding remarks are finally drawn in Section 5.

2. Analysis of the considered negative stiffness nonlinear oscillator

The NSN oscillator design is shown in Fig. 1(a). It should be noted that the function of the oscillator is rather different compared to previous work [43, 67] which were aiming at vibration isolation for a single degree of freedom system and for which a positive stiffness was also required to support the weight of the oscillating mass.

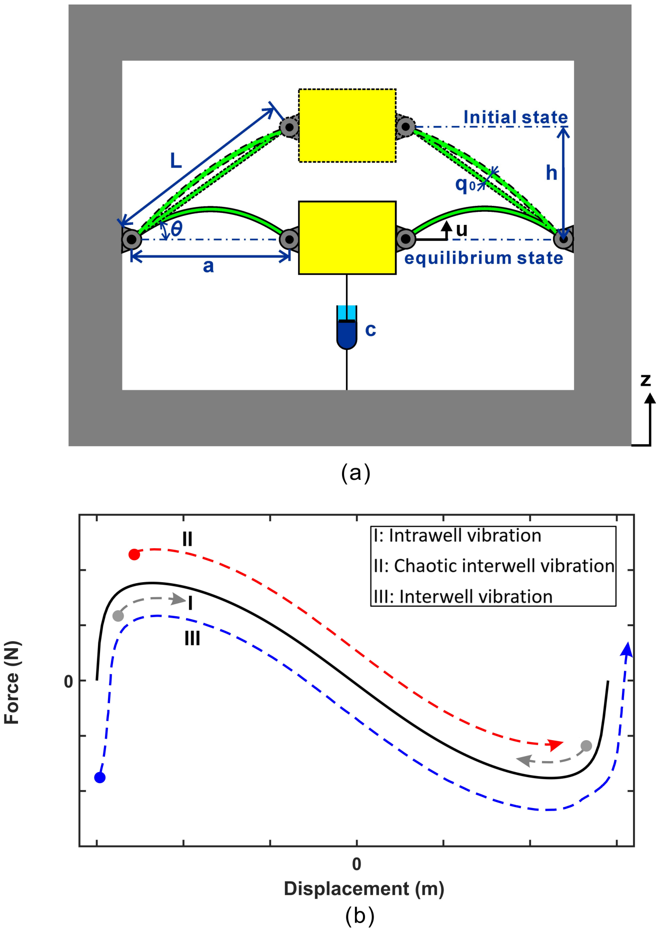

Figure 1: (a) The employed NSN oscillator depicted enclosed within the master structure (not to scale). The upper stable, as well as the snap-through (unstable equilibrium) states are shown along with the considered design variables of the oscillator, (b) The three expected vibration modes of the oscillator: I. Intrawell stable oscillation, II. Chaotic interwell oscillation and III. High amplitude interwell oscillation.

In this work the NSN comprises a small mass m_{osc} which is destined to oscillate with a significant amplitude to maximize the absorbed vibrational energy. The kernel idea to explore in this work is employing an unstable spring which will push m_{osc} away from its equilibrium position to maximize vibration amplitude. There are typically three oscillation modes for the NSN oscillator, i.e. intrawell vibration which is the low amplitude oscillation that cannot cross the equilibrium state, chaotic interwell vibraiton which has medium amplitude that is able to cross the equilibrium state and interwell vibration with largest oscillation amplitude as shown in Fig. 1(b).

The considered values for m_{osc} will be relatively low (5-10%) compared to the master structure thus the inertial forces applied on m_{osc} due to acceleration are expected to be much larger than weight. This is in contrast to previous works [18, 41, 43, 45, 67, 68] where a large mass is supported by a positive stiffness spring and the vibration of which is to be abated in order to minimize transmissibility. Such transmissibility isolation devices incorporating Euler buckled beams have been employed for increasing driver seat comfort, as well as satellite vibration isolation bases. In this work the authors adopt this design concept and aimed at adapting its design variables to transform it into a vibration absorption oscillator. Fig. 2 illustrates this major difference in the two designs (vibration isolation and vibration absorption), stressing the fact that optimal operation range for transmissibility isolation is focused around the equilibrium point of the Euler beams, while in this work the authors are attempting full interwell vibration for m_{osc} in order to maximize the amount of absorbed energy.

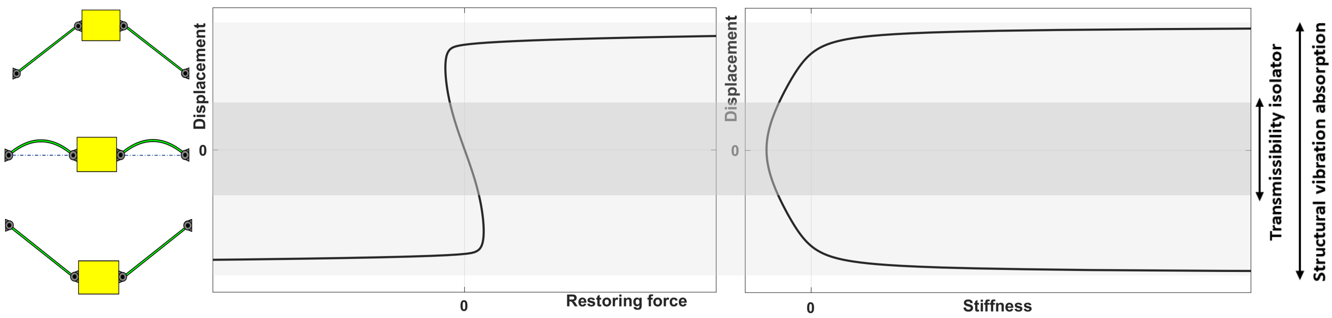

Figure 2: Representative force-displacement and stiffness-displacement curves are presented next to the corresponding positions of the oscillating mass. The targeted operating zones are also presented, highlighting the difference between operation of a single degree of freedom transmissibility isolator connected to a heavy mass [43] (dark grey) and the structural vibration absorption configuration (light grey) proposed in this work.

Another major difference between this work and previous ones is that the NSN oscillators are hereby not designed for improved functionality close to zero frequency but for activation close to structural resonances around which vibration amplitude becomes maximum. The optimal design is therefore not necessarily the one providing zero stiffness for m_{osc} but the one that maximizes energy absorption close to resonances thanks to sufficient inertial restoring force which allows for m_{osc} to perform interwell vibration. This is typically attained at frequencies higher than 0, as well as high structural vibration amplitudes.

2.1. Derivation of the frequency response curve expression for the proposed NSN oscillator under a master structure displacement excitation

The perpendicular normalized force transmitted from the axially loaded slender beam to the oscillating mass can be provided by the solution of the Euler beam expression [40, 69] as

$$\frac{F}{P_e} = \left[1 - \frac{\pi q_0}{L}\left(\left(\frac{\pi q_0}{L}\right)^2 + 4\left(1 - \sqrt{\left(\frac{u}{L}\right)^2 + (\cos\theta)^2}\right)\right)^{-1/2}\right] \times \left[\sqrt{\left(\frac{u}{L}\right)^2 + (\cos\theta)^2} - \frac{12 + \left(\frac{\pi q_0}{L}\right)^2}{4}\right]\left[\frac{u}{L\sqrt{\left(\frac{u}{L}\right)^2 + (\cos\theta)^2}}\right] \tag{1}$$

with q_0 being the initial imperfection of the beam, L its initial length before buckling,

$$P_e = EI\frac{\pi^2}{L^2} \tag{2}$$

E being the Young's modulus of the beam material and I the second moment of area for the beam's cross-section. It is worth noting that when the two endpoints of the beam lay on a horizontal line (u=0) it is implied that the vertical restoring force the two beams are providing is zero with the corresponding restoring stiffness also being minimum at that state of unstable equilibrium (see also Fig. 2). The vertical restoring force is symmetric about that point.

A Taylor Series expansion of the restoring force determined by Eq.(1) can be formulated around the unstable equilibrium point (u=0), as

$$\frac{F}{P_e} = -k'_1\left(\frac{u}{L}\right) + k'_3\left(\frac{u}{L}\right)^3 , \tag{3}$$

which can be reduced to the following system of equations

$$F = -\left(\frac{k'_1 P_e}{L}\right)u + \left(\frac{k'_3 P_e}{L^3}\right)u^3 = -k_1 u + k_3 u^3, \tag{4}$$

with

$$k'_1 = (\frac{a-b}{2a\gamma})(\frac{b^2}{2} - 2\gamma + 6) \tag{5a}$$

$$k'_3 = \frac{a-b}{2a\gamma^2} + (\frac{a-b}{4\gamma^3 a} + \frac{b}{2\gamma^2 a^3})(\frac{b^2}{2} - 2\gamma + 6) \tag{5b}$$

$$a = \sqrt{\left(\frac{\pi q_0}{L}\right)^2 - 4\cos\theta + 4} \tag{5c}$$

$$b = \frac{\pi q_0}{L} \tag{5d}$$

$$\gamma = \frac{a}{L} = \cos\theta \tag{5e}$$

Following Figs.1 and 2, the mass may be balanced at $u = +u_0$ or $u = -u_0$, which is determined by the characteristics of the Euler beam and the ones of the oscillating mass

$$-k_1u_0 + k_3u_0^3 = mg \tag{6}$$

where $u = +u_0$ can be solved by Cardano method. The balanced position as well as the number of solutions are determined by whether $\Delta{=}\left(-\frac{mgL^3}{2k_3'P_e}\right)^2 + \left(-\frac{k_1'L^2}{3k_3'}\right)^3 = \left(\frac{mg}{2P_e}{+}\frac{k_1'}{3}\sqrt{\frac{k_1'}{3k_3'}}\right)\left(\frac{mg}{2P_e} - \frac{k_1'}{3}\sqrt{\frac{k_1'}{3k_3'}}\right)$ is larger, equal to or smaller than zero.

The equation of motion for the single degree of freedom system is therefore expressed as

$$m\frac{d^2y}{dt^2} + c\frac{dy}{dt} - k_1\left(y{+}u_0\right) + k_3\left(y{+}u_0\right)^3 = mZ_0\omega^2\cos\omega t + mg, \tag{7}$$

with $y = u - z$ being the relative displacement and Z_0 the vibration amplitude of the master structure. Then according to Eq. (6) and (7), the equation of motion becomes

$$m\frac{d^2y}{dt^2} + c\frac{dy}{dt} + \left(-k_1 + 3k_3u_0^2\right)y + 3k_3u_0y^2 + k_3y^3 = mZ_0\omega^2\cos\omega t, \tag{8}$$

or

$$\frac{d^2y}{dt^2} + \frac{c}{m}\frac{dy}{dt} + \frac{\left(-k_1 + 3k_3u_0^2\right)}{m}y + \frac{3k_3u_0}{m}y^2 + \frac{k_3}{m}y^3 = Z_0\omega^2\cos\omega t. \tag{9}$$

The above equation is written in a general way as

$$\ddot{y} + 2\beta\dot{y} + \alpha_1y{+}\alpha_2y^2 + \alpha_3y^3 = Z_0\omega^2\cos\omega t \tag{10}$$

where

$$\beta = \frac{c}{m} \tag{11a}$$

$$\alpha_1 = \frac{-k_1 + 3k_3u_0^2}{m} \tag{11b}$$

$$\alpha_2 = \frac{3k_3u_0}{m} \tag{11c}$$

$$\alpha_3 = \frac{k_3}{m} \tag{11d}$$

The harmonic balance method [70] is employed to get the steady solution for the response of the system. The steady-state solution to Eq. (10) is assumed to be $y\left(t\right) = A_0 + A_1\cos\left(\omega t + \varphi\right)$ and by setting the coefficients of the same harmonics to be equal and ignoring the higher harmonics leads to

$$b_1A_0 + b_3A_0^3 + \frac{3}{2}b_3A_0A_1^2 = b_0 \tag{12a}$$

$$-\omega^2A_1 + b_1A_1 + 3b_3A_0^2A_1 + \frac{3}{4}b_3A_1^3 = Z_0\omega^2\cos\varphi \tag{12b}$$

$$-2\beta\omega A_1 = Z_0\omega^2\sin\varphi \tag{12c}$$

where

$$b_0 = \frac{\alpha_1\alpha_2}{3\alpha_3} - \frac{2\alpha_2^3}{27\alpha_3^2} \tag{13a}$$

$$b_1 = \alpha_1 - \frac{\alpha_2^2}{3\alpha_3} \tag{13b}$$

$$b_3 = \alpha_3. \tag{13c}$$

Then combining Eqs.(12) to give the implicit equation for the amplitude of the constant term A_0 we get

$$\begin{aligned} 25b_3^3A_0^9 + \left(35b_1b_3^2 - 20\omega^2b_3^2\right)A_0^7 - 15b_0b_3^2A_0^6 + \left(11b_1^2b_3 + 4\omega^4b_3 + 16\zeta^2\omega^2b_3 - 24b_1b_3\omega^2\right)A_0^5 \\ + \left(2b_0b_1b_3 + 16\omega^2b_0b_3\right)A_0^4 + \left(b_1^3 - 4b_1^2\omega^2 + 4\omega^4b_1 + 16\beta^2\omega^2b_1 - 9b_0^2b_3 + 6b_3Z_0^2\omega^4\right)A_0^3 \\ + \left(b_0b_1^2 - 4\omega^4b_0 - 16\beta^2\omega^2b_0\right)A_0^2 + \left(4b_0^2\omega^2 - b_0^2b_1\right)A_0 - b_0^3 = 0. \end{aligned} \tag{14}$$

According to Eq.(14), A_0 can be obtained for a given value of b_0, b_1, b_3, Z_0 and β. Then the harmonic term A_1 is obtained by Eq.(12a). The variation of the bias term A_0 as a function of frequency ω is solved by employing Eqs.(12).

$$\frac{8\beta^2\left(b_0 - b_1A_0 - b_3A_0^3\right)}{3b_3A_0}\omega^2 + A_1\left(-\omega^2 + \frac{b_1}{2} + \frac{5}{2}b_3A_0^2 + \frac{b_0}{2A_0}\right)^2 = Z_0^2\omega^4 \tag{15a}$$

$$A_1 = \frac{2\left(b_0 - b_1A_0 - b_3A_0^3\right)}{3b_3A_0}. \tag{15b}$$

The frequency response curves (FRCs) of A_1 are solved by Eq.(12a) after A_0 is obtained as a function of frequency ω. The locus of the peak amplitudes of the bias term A_{0p} is obtained by the fact that it happens at $\phi=\pi/2$, thus

$$\omega_0^2 = \frac{b_1}{2} + \frac{5}{2}b_3A_0^2 + \frac{b_0}{2A_0}. \tag{16}$$

The peak response of the bias term, named as A_{0p}, is determined through

$$\begin{aligned} &\left(80\beta^2b_3^2 + 75Z_0^2b_3^3\right)A_{0p}^6 + \left(96\beta^2b_1b_3 + 30Z_0^2b_1b_3^2\right)A_{0p}^4 - \left(64\beta^2b_0b_3 - 30Z_0^2b_0b_3^2\right)A_{0p}^3 \\ &+ \left(16\beta^2b_1^2 + 3Z_0^2b_1^2b_3\right)A_{0p}^2 + 6Z_0^2b_0b_1b_3A_{0p} - 16\beta^2b_0^2 + 3Z_0^2b_0^2b_3 = 0. \end{aligned} \tag{17}$$

After solving Eq.(17) for A_{0p}, the value is substituted in Eq.(16) to obtain the peak frequency, and then the peak response of the harmonic term A_{1p} is obtained by Eq.(12).

According to Descartes's rules of signs [71], the number of positive roots of the real algebraic equation, i.e. Eq.(14), is either equal to the number of sign changes in the sequence of the coefficients of the polynomial, or less than that number by a positive even integer. By considering this theorem, the system of Eq.(14) can have a maximum number of one, three or five steady-state values. It should be pointed out that, although the number of sign changes in the sequence of the coefficients of the polynomial is only three for counting the 'positive' and 'negative' signs, the actual number of sign changes is dependent on the outcome of the coefficients, which are functions of b_0, b_1, b_3, Z_0 and β. The multivaluedness implies the occurrence of a multiple jump phenomenon.

2.2. Stability of the approximate harmonic balance solution

In the case where there are several stationary values, it is necessary to analyze the stability of the approximate harmonic balance solution due to the fact that not all of them will correspond to stable motion. To perform this stability analysis, a small perturbation $\chi(\tau)$ is introduced to the assumed solution

$$y^{*}(t) = A_0 + A_1 \cos(\omega t + \varphi) + \chi(\tau). \tag{18}$$

Substituting Eq.(18) in Eq.(10), we obtain the corresponding linearized variational expression

$$\frac{d^2\chi}{d\tau^2} + 2\beta\frac{d\chi}{d\tau} + b_1\chi + 3b_3\left(A_0 + A_1\cos(\omega t + \varphi)\right)^2\chi = 0. \tag{19}$$

Using the substitution $\chi(\tau) = e^{-\upsilon\tau}\eta(\tau)$, Eq.(10) is transformed into Hill's equation written as

$$\frac{d^2\eta}{d\tau^2} + \left(\left(-\beta^2 + b_1 + 3b_3A_0^2 + \frac{3}{2}b_3A_1^2\right) + 2\left[3b_3A_0A_1\cos(\omega t + \varphi) + \frac{3}{4}b_3A_1^2\cos(2(\omega t + \varphi))\right]\right) = 0. \tag{20}$$

Taking $\sigma_0 = -\beta^2 + b_1 + 3b_3A_0^2 + \frac{3}{2}b_3A_1^2$, $\sigma_1 = 3b_3A_0A_1$, $\sigma_2 = \frac{3}{4}b_3A_1^2$, and following the procedures available in the literature [72] and based on the Floquet theory, the stability condition follows as

$$\sigma_0\sigma_2^2 - 2\sigma_1^2\sigma_2 + 2\sigma_1^2(\sigma_0 - \Omega^2) - \sigma_0(\sigma_0 - \Omega^2)^2 > 0. \tag{21}$$

When three steady states occur in the system for a single frequency two of them are stable and one unstable. Moreover, where five steady states occur then three of them are stable and two unstable.

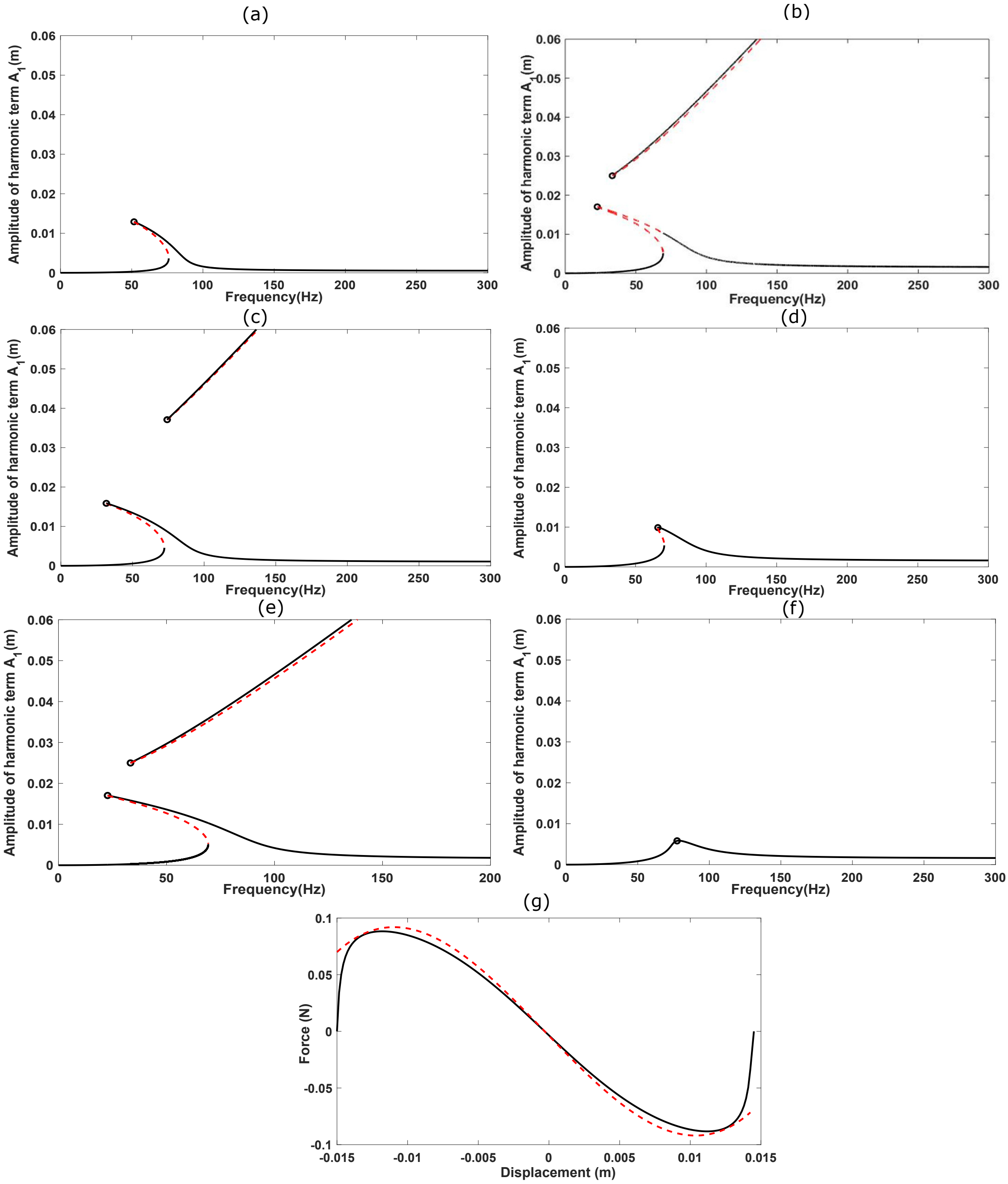

Figure 3: Frequency response curves for the considered NSN oscillator having m_{osc}=0.004kg, h=0.015m, q_0=0.001, L=0.021m, EI=4$\times10^{-6}$GPam^4. In the left column subfigures (a), (c) and (e) present results for increasing vibration amplitude of the master structure from Z_0=1mm then Z_0=5mm and eventually Z_0=10mm for a constant damping coefficient c=0.01kg/sec. In the right column subfigures (b), (d) and (f) present results for increasing vibration amplitude of the master structure from Z_0=1mm then Z_0=5mm and eventually Z_0=10mm for a constant damping coefficient c=0.05kg/sec. Unstable part of the frequency response curves in ($--$) and red line style and colour. Subfigure (g) presents a comparison between the approximated force-displacement relation implemented in Eq.(9) ($--$) against the complete analytical expression of the restoring force in Eq.(1) (-) for the design presented in the above subfigures.

Fig. 3 depicts the frequency response curves for a variety of designs of the single degree of freedom NSN oscillator. For the nonlinear system under investigation it is known that the excitation amplitude and damping are primary candidates to affect its response [73] and are therefore hereby investigated. Results are presented for three levels of master structure's excitation, as well as for two level of damping values for the viscous element connected to m_{osc}. In Fig. 3 the dotted parts represent the unstable regions. When there are three steady states occurring in the system for a single frequency, two of them are stable and one unstable. The results are in good agreement with intuitionally expected behaviour (interwell oscillation branch moving to lower frequencies with increase of basis oscillation amplitude and with decrease of damping), as well as with the explicit transient calculations exhibited in Sec.2.2.

It is observed that an increase of the damping coefficient c results in decrease of the oscillation amplitude for m_{osc}. Simultaneously, the frequency at which m_{osc} enters interwell vibration increases which is disadvantageous for absorbing energy at low frequency spectra. The designer should therefore balance the decreased oscillation amplitude against the benefits of increasing c before determining the optimal level of damping for the oscillator. When Z_0 varies with c remaining constant, it is also observed that increasing the vibration amplitude of the master structure results in an increased oscillation amplitude for m_{osc}. The activation frequency for interwell vibration also shows to decrease with an increase of Z_0 which suggests that large vibration amplitudes should be beneficial for harvesting energy out of the master structure. An issue however later identified (see Sec.3.4) is that as the master structure obtains large quantities of vibrating energy, the portion of the energy damped by the interwell oscillation actually reduces with simultaneous reduction of the effective global dissipation factors.

In the same Fig. 3 a comparison is presented between the approximated buckled beam restoring force implemented in Eq.(9) against the complete analytical expression of the force in Eq.(1). It is shown that the Taylor expansion provides an overall good approximation, however due to the large oscillation amplitudes of m_{osc} deviations are to be expected between the solution of Eq.(9) and the explicit transient solution taking the full Eq.(1) into account. The above presented analytical tool can therefore be employed as an efficient preliminary design optimization tool for providing satisfactory approximations on the amplitude of oscillation and the interwell activation frequencies of specific designs. Such efficient tools are essential for performing fast searches on the design space given that seven design variables are to be considered for the oscillator.

2.3. Analysis of the NSN oscillator through an explicit time integration scheme

It is reminded that interwell vibration is desired for the NSN oscillator. Unfortunately, while a Taylor expansion is generally adequate for capturing the response of the system close to its unstable equilibrium position [43], its predictions for an intensely fluctuating force (such as the one presented in Fig. 2) can deviate away from $u = 0$ with a consequent impact on the accuracy of the approximated expressions derived in Sec.2.1. As a subsequent step, the fundamental force-displacement equation for an Euler buckled beam in Eq. (1) describing the oscillator in Fig. 1 is explicitly solved through a time integration scheme in order to investigate the transient behaviour of the system. A basis excitation is imposed and the displacement of the mass is computed in the time domain.

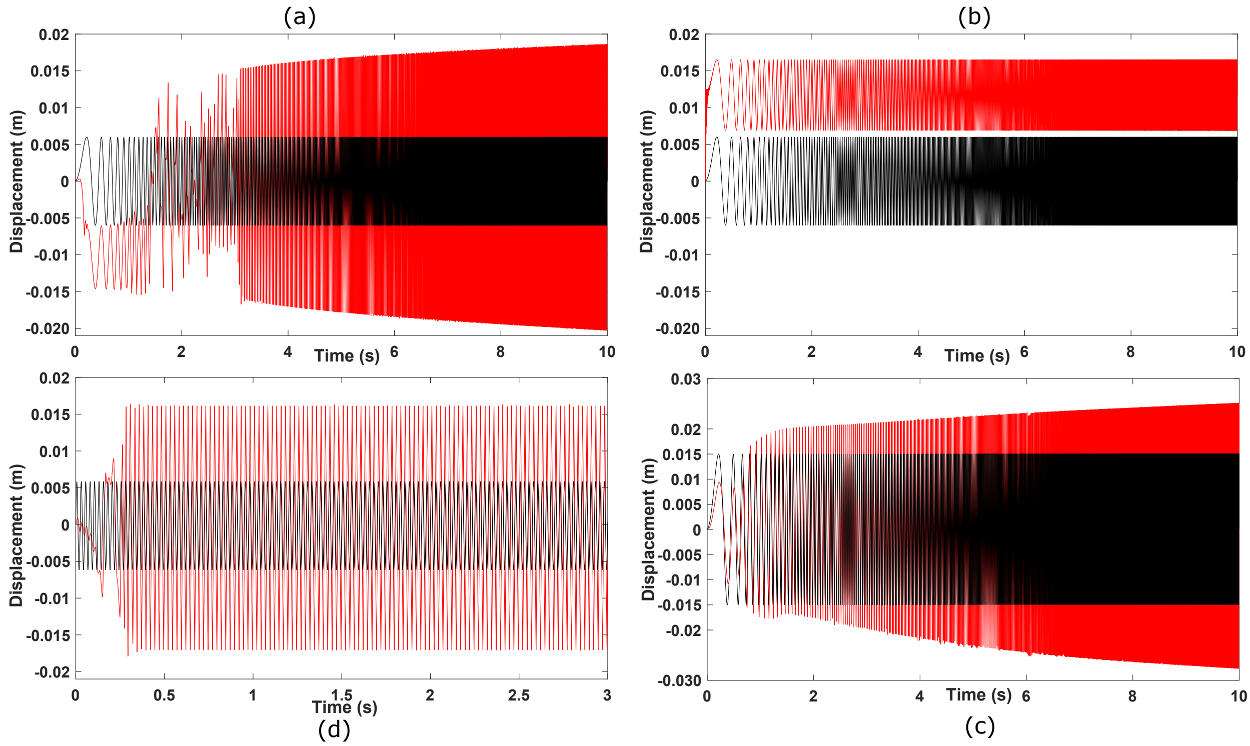

Figure 4: Response of the oscillating mass (shown in red) for an input base excitation (shown in black). All results are computed with a resolution of 0.0001sec to ensure adequate discretization in the time domain. Clockwise from upper left: (a) Response of a NSN oscillator tuned to operate after 30Hz to a linear chirp base excitation having Z_0=0.006m scanning a frequency range of f_{min}=0.1Hz to f_{max}=100Hz in 10 seconds. (b) Response of a mistuned oscillator having excessive beam stiffness not allowing for interwell motion. The excitation is a linear chirp having Z_0=0.006m scanning a frequency range of f_{min}=0.1Hz to f_{max}=100Hz in 10 seconds.(c) Response of an oscillator tuned to operate after 30Hz to a linear chirp base excitation having Z_0=0.015m scanning a frequency range of f_{min}=0.1Hz to f_{max}=100Hz in 10 seconds. (d) Typical steady-state response of an oscillator tuned to operate after 30Hz to a sinusoidal base excitation having Z_0=0.006m and a constant frequency of 40Hz.

The principal goal of this subsection is to investigate the designs that are able to perform interwell oscillation. As observed in Fig. 3, the increase of the master structure vibration amplitude, as well as the decrease of damping are expected to facilitate interwell oscillation. It is however hereby stressed that the goal of vibration absorption devices is dissipating the largest *portion* of energy, that is achieving a maximum dissipated energy ratio defined as

$$\eta = \frac{E_{diss}}{E_{struc}} \tag{22}$$

with E_{diss} the amount of energy dissipated by the mechanism and E_{struc} the vibrational energy of the master structure. Given that the increase of c could simultaneously facilitate the increase of E_{diss} and impede interwell vibration of m_{osc} it is evident that a proper design optimization of the NSN oscillator design would be required to achieve optimal absorption performance. Another point to consider is that the maximum oscillation amplitude for m_{osc} is constrained by the design of the master structure with typical composite sandwiches having thicknesses of the order of a few centimeters. The maximum value of E_{diss} is therefore following a similar constraint. While an important Z_0 is desired to activate interwell oscillation for m_{osc}, a very large value for Z_0 would increase E_{struc} and therefore result in a low η for the NSN absorption design. For very high Z_0 values of the master structure vibration, vibroimpact effects may take place (between m_{osc} and structural facesheets) necessitating dedicated analysis techniques [74–76] and further complicating response predictions.

Results from the explicit time integration scheme are exhibited in Fig. 4 for a variety of designs. The ode45 MATLAB function is employed which is based on a fourth-order accurate explicit Runge-Kutta method. The choice of time step was made such that at least 100 points are calculated per cycle. It is observed in Fig. 4(a) that the system can be designed to perform interwell oscillation for a broadband frequency range. Results are shown for design variables: m_{osc}=0.004kg, c=0.05kg/sec, h=0.015m, q_0=0.001, L=0.021m, EI=4×10^{-6}GPam^4. As expected, an increase of vibration amplitude increases the interwell vibration spectrum. It was found particularly challenging to come up with a design that induces interwell vibration close to zero frequency due to the need for a substantial inertial force to overcome the snap-through threshold. The frequency scan from f_{min}=0.1Hz to f_{max}=100Hz showed that interwell vibration above about 30Hz can be attained in a straightforward manner given the aforementioned dimension constraints. For the same design, the steady state response to a monotonic sinusoidal excitation of 40Hz is provided for the sake of completeness in Fig. 4(d). It is observed that the motion of m_{osc} quickly converges to a steady-state response of the same frequency as the one of the master structure within a few cycles.

2.4. Performance of a mistuned mechanism

In Fig. 4(b) results for a mistuned design are presented having m_{osc}=0.004kg, c=0.05kg/sec, h=0.015m, q_0=0.001, L=0.021m, EI=4×10^{-3}GPam^4. By 'mistuning' we imply any design conditions that impede interwell oscillations of m_{osc}. Mistuning can result either from excessive damping or excessive stiffness of the employed beam structures which will not allow m_{osc} to perform full interwell oscillation. The result clearly shows m_{osc} moving from the initial unstable equilibrium state to one of the extreme positions and performing intrawell vibration around that position for the entire scanned spectrum. Such a mode of vibration implied reduced energy absorption.

In Fig. 4(c) it is observed that increasing the oscillation amplitude close to the design value h implies interwell vibration for the oscillating mass starting at a very low frequency range (in this case at less than 5Hz). Results are shown for m_{osc}=0.004kg, c=0.05kg/sec, h=0.015m, q_0=0.001, L=0.021m, EI=4×10^{-6}GPam^4 and a structural vibrating amplitude of Z_0=15mm. The increase of the vibrating amplitude of the oscillating mass y_0 however is not proportional to the increase of Z_0. This fact implies reduced normalised energy absorption η which suggests that such a design would be considered to be underperforming. It is therefore clear that the thickness of the sandwich and therefore the available maximum vibration amplitude for m_{osc} has major impact on the overall performance of the absorption system. This is nothing surprising, also being an important limitation for linear oscillator designs. The impact of vibration amplitude on the damping performance of the employed oscillators is investigated further in Sec.3.4.

3. Implementation of NSN oscillators within a vibrating multilayered sandwich structure

In this section the NSN oscillators will be numerically implemented within a vibrating sandwich master structure to evaluate their performance as an energy absoprtion system focusing around the two first structural resonances.

The sandwich structure is made up by a periodic unit cell. A total of 8×8 repetitions of the unit cell in the x and y directions form the full sandwich panel. The unit cell has dimensions L_x=0.09m, L_y=0.06m, while h_c=0.035m is the core thickness and h_f=0.001m is the thickness of each facesheet. As shown in Fig.5 a void is implemented within each unit cell equal to one third of the corresponding dimensions in the x and y directions within which the NSN oscillator is implemented. The material characteristics for the master structure are E_f=70GPa for the facesheets, E_c=0.07GPa for the core material, v_f=0.1 for the facesheets, v_c=0.3 for the core, ρ_f=3000kg/m^3 for the facesheets, ρ_c=50kg/m^3 for the core, while both the core and the facesheet materials have a structural damping loss factor equal to 1%. The implemented NSN oscillators have m_{osc}=0.004kg, c=0.05kg/sec, h=0.015m, q_0=0.001, L=0.021m and EI=4×10^{-6}GPam^4. This NSN design was selected after an extensive parametric study thanks to its capacity to start performing interwell vibration at a frequency below the first structural resonance (below 35Hz).

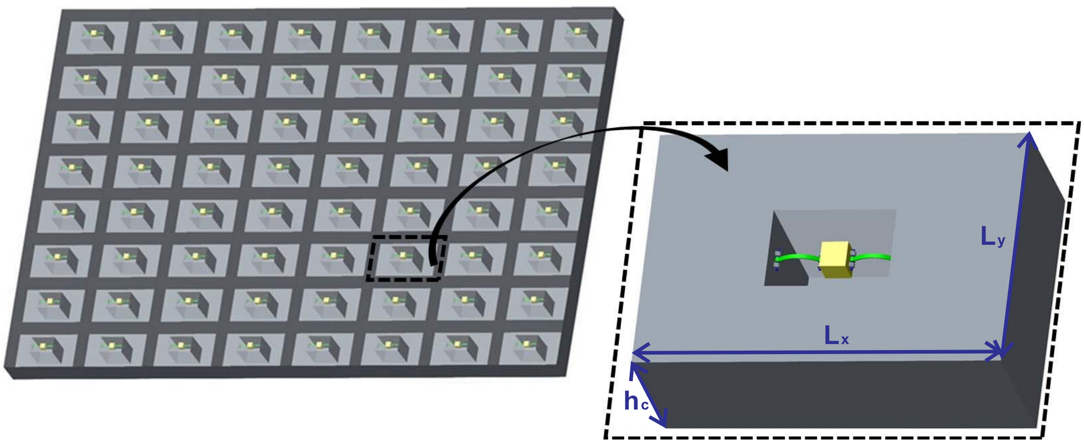

Figure 5: Caption of the sandwich structure and its unit cell incorporating the negative stiffness oscillator. Upper facesheet of the sandwich panel is omitted for clarity.

The sandwich structure is modelled through solid, linear brick finite elements (FEs) with nonlinear spring-mass dampers being implemented to simulate the behaviour of the NSN oscillators within each unit cell. The coincident nodes of the nonlinear spring mass elements are merged to the ones of the master structure. The structural response is computed through an explicit time domain solution employing the ANSYS FE platform. A chirp displacement function scanning a frequency range between f_{min}=0.1Hz to f_{max}=100Hz with a force amplitude equal to 150N is injected at position x=0.18m, y=0.12m of the sandwich structure. The four corners of the panel are clamped to have zero displacement boundary conditions.

3.1. Dynamic response of the master sandwich structure

Two approaches are employed to extract the response of the nonlinear system. To provide results in an efficient manner, the FRF of the structure is initially determined through an H_1 estimate by Welch's method applied on the chirp signal results. Moreover, the steady-state response is computed under a signal containing 10 cycles of a chirp function from f_{min}=0.1Hz to the targeted frequency, followed by 90 cycles of monotonic sinusoidal excitation. The initial chirp was implemented in order to avoid impact effects in the beginning of the simulation. The steady-state response function is evaluated by applying a spectral density estimation on the last 30 cycles of the computed response. Results under both excitation types are presented in Fig. 6. The outcome of the Welch's method is in excellent agreement with the steady-state sinusoidal excitations which are considered more reliable as an index and will be employed in the remainder of the work. Results obtained through the Welch's method show intense fluctuations towards the end of the analysed spectrum, suggesting that the excited harmonics start having important effect on the obtained chirp signal after about 80Hz. Computational effort for this 29,558 degree of freedom FE problem were rather intensive with about 330 minutes required for each sinusoidal steady-state result ($\diamond$) and 1390 minutes required for the evaluation of the chirp output on a standard 2.2GHz processor having 8GB of RAM memory.

The equivalent linear systems having the same multilayered sandwich structure, as well as the same m_{osc} are subsequently considered as references. It is well known that such mechanical metastructures with linear oscillators [77, 78] have excellent vibration absorption properties around targeted, narrow frequency spectra, widely known as stopbands. The same transient linear chirp signal and the same Welch's approach were employed to obtained the frequency response functions of the linear structures. Three scenarios are considered as follows: i) the linear resonators being tuned at a frequency of 170Hz (higher than the first two structural resonances and outside the displayed range of interest), ii) tuned on the 1^{st} structural resonance and iii) tuned on the 2^{nd} structural resonance. In Fig. 7(a) results are exhibited for the system comprising linear oscillators tuned at a frequency above the two first modes. It is observed that the sandwich structure with NSN oscillators has smaller fluctuations in the FRF curve than that with linear oscillators. The NSN system hence outperforms its linear counterpart in a broadband sense with differences of over an order of magnitude being observed with regard to induced displacement amplitudes close to the excitation point.

To add more interest to the comparison, results are exhibited in Figs. 7(b),(c) for the linear oscillators being tuned on the 1^{st} and 2^{nd} structural resonances respectively. The internally oscillating mass has been kept constant in all cases in order to render the designs

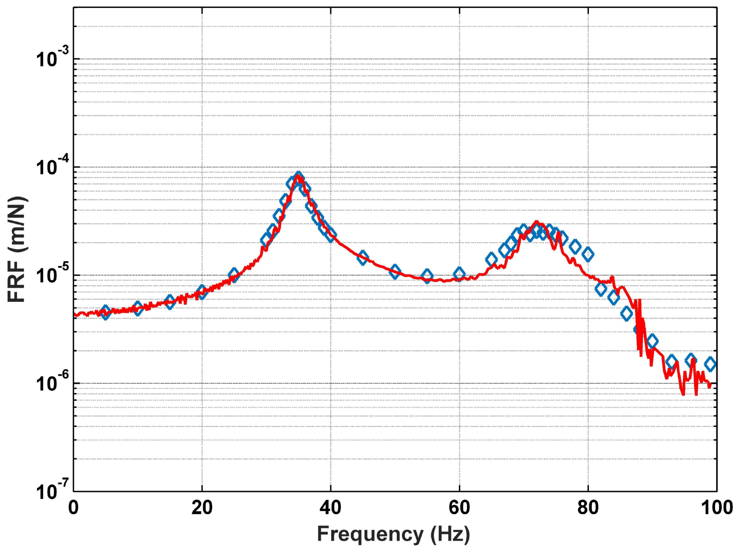

Figure 6: Structural response at x=0.54m, y=0.12m. Red lines exhibit results for a linear chirp excitation scanning a range between f_{min}=0.1Hz to f_{max}=100Hz. Steady-state response to monotonic sinusoidal excitations are also presented in $\diamond$.

comparable to each other. The stiffness of the spring has been altered for the linear tuned mass dampers in order to target the desired resonance frequency of the panel. As expected, the locally resonant linear sandwich structures are exhibiting stopbands at the corresponding tuning frequencies. Structural response turns much lower within these narrow ranges, implying that for monotonic excitations a linear oscillator design would be most appropriate. Due to the well known emerging side resonances [79, 80] however the performance of the linear design is highly compromised with the maximum response in the region exceeding the one for the NSN design. It is widely known that 'erasing' these side resonances high damping values for the linear oscillators (typically a damping ratio over 20%) or special active treatments need to be implemented. This need further compromises the practicality of the linear design.

On the other hand, the NSN design presents an improved performance in a broadband sense. A single periodic oscillator type with a low amount of damping induces reduction of structural vibration by more than an order of magnitude, both around the 1^{st} and 2^{nd} structural resonances. The response is also lower than the side resonances induced by the stopbands of the linear design.

3.2. Dynamic response of the internal mechanism

To provide further insight into the response of the system comprising NSN oscillators, steady-state responses of the system under a sinusoidal monotonic excitation are provided in Fig. 8. Two cases, below and above 30Hz are distinguished with the NSN oscillators performing intrawell (f=10Hz) and interwell (f=35Hz) oscillation respectively. Going back to the frequency response functions of the system in Fig. 7 it is now clearly observed that interwell oscillation increases the apparent structural damping in comparison to the equiv-

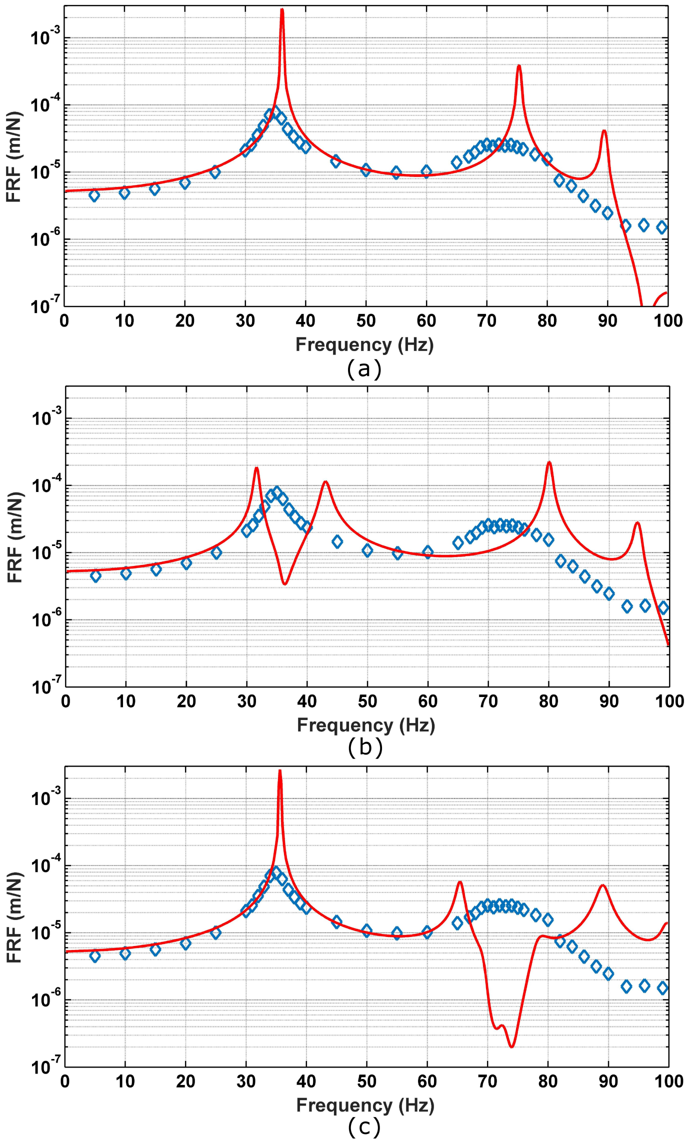

Figure 7: Structural response at x=0.54m, y=0.12m. (a) Comparison between the NSN design $\diamond$ and the linear design with oscillators tuned higher than 100Hz. (b) Comparison between the NSN design $\diamond$ and the linear design with linear oscillators tuned at the first structural resonance. (c) Comparison between the NSN design $\diamond$ and the linear design with oscillators tuned at the second structural resonance.

alent linear system and has beneficial desired effects conjectured in the beginning of this manuscript.

It should be stressed that the time resolution in Fig. 8 is equal to 20 instants per cycle, therefore the intense dynamics observed during the interwell oscillation of m_{osc} are by no means related to noise. Further increasing the time resolution would provide a slightly smoother time domain response, without altering the impact of the NSN mechanisms on global structural damping.

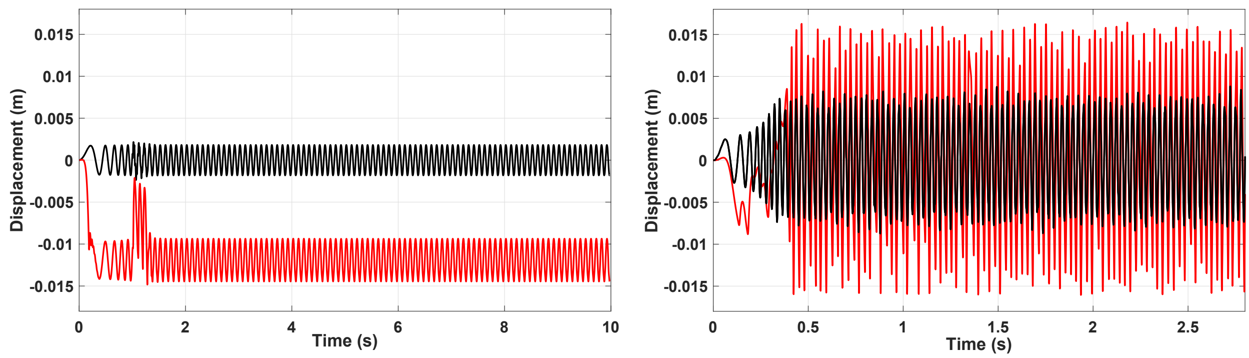

Figure 8: Typical waveforms obtained through an explicit transient FE solution. Response at x = 0.54m, y = 0.12m. The NSN design has m_{res}=0.004kg, c=0.05kg/sec, h=0.015m, q_0=0.001, L=0.021m, EI=4×10^{-6}GPam^4. Red curves represent the displacement of the oscillating mass, while black curves represent the master structure response at the same position. Left: Response for 10 cycles of a chirp function from f_{min}=0.1Hz to f_{target}=10Hz, followed by 90 cycles of monotonic sinusoidal excitation at f_{target}. It is observed that the oscillator is still operating at intrawell motion. Right: Response for 10 cycles of a chirp function from f_{min}=0.1Hz to f_{target}=35Hz, followed by 90 cycles of monotonic sinusoidal excitation at f_{target}. The interwell motion of the NSN oscillator has been activated at that frequency.

3.3. Parametric study on the performance of the structural system with respect to the mechanism's damping coefficient

It is important to investigate the performance of the implemented oscillators vis-à-vis the level of added viscous damping c. For the master structure's components, it is reminded that both the core and the facesheet materials have a structural damping loss factor equal to 1%. As discussed in Sec.2, increase of damping is expected to reduce the amplitude of the oscillation of m_{osc}, while on the other hand it would facilitate the absorption of additional energy by the oscillators. In Fig. 9 a parametric study is exhibited, investigating the structural response level at the first natural frequency of the master structure. Response at $x = 0.54$m, $y = 0.12$m of the master structure is depicted with other nodal coordinates of the structure presenting a very similar behaviour. The same forcing input as above is employed.

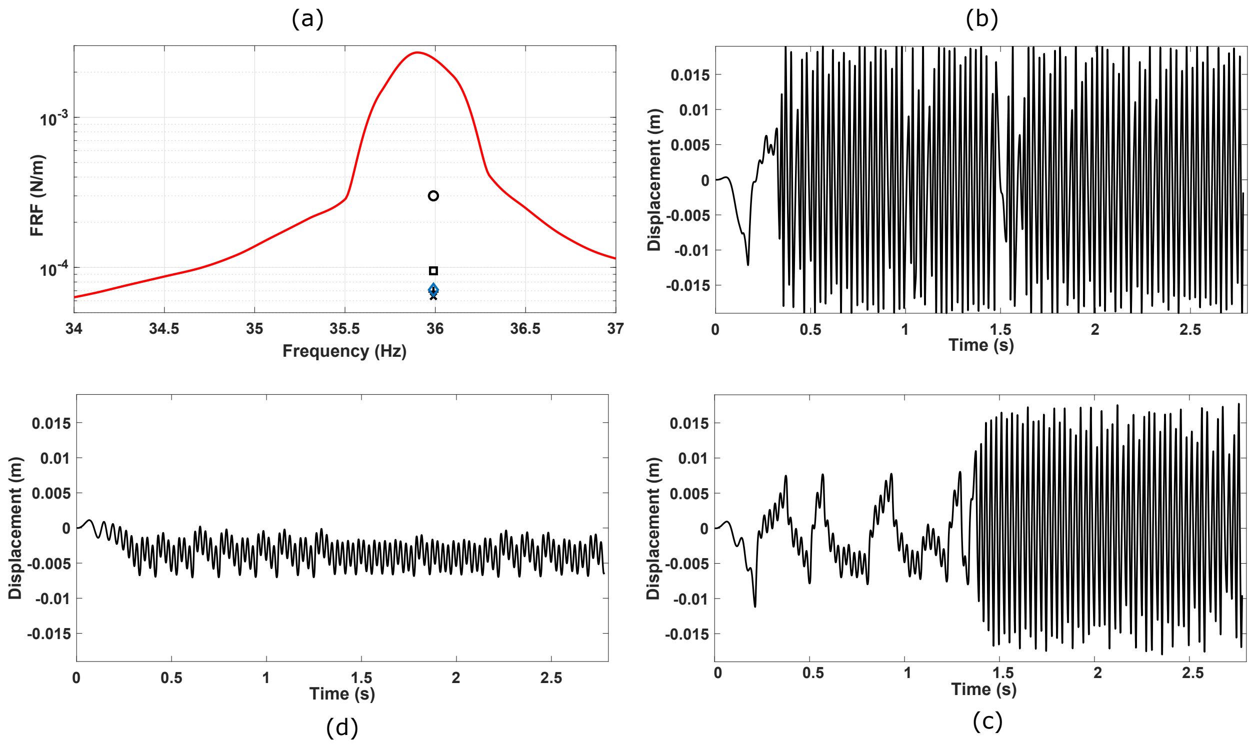

Figure 9: Parametric study of the structural response at the first natural frequency of the sandwich panel with respect to the oscillators damping coefficient c. The oscillator has m_{res}=0.004kg, h=0.015m, q_0=0.001, L=0.021m, EI=4×10^{-6}GPam^4: (a) The response in the frequency domain shown at 36Hz for c=0.005kg/sec (□), c=0.01kg/sec (x), c=0.025kg/sec (+), c=0.05kg/sec (⋄) and c=0.15kg/sec (o). (b) Typical transient waveform for m_{osc} when c=0.005kg/sec, (c) Typical transient waveform for m_{osc} when c=0.05kg/sec, (d) Typical transient waveform for m_{osc} when c=0.15kg/sec.

Having a look at the waveform signatures for m_{osc}, it can be observed that for a very low viscous damping value, the oscillator enters interwell vibration after a few cycles and oscillates at a high amplitude within the cavity. Despite the high amount of energy stored in m_{osc}, as seen in Fig. 9(a) the overall performance of the design is not optimal since a minimum amount of that energy is damped by the viscous element. Increasing damping at the area of c=0.01-0.05kg/sec seems to optimise the structural performance. Moreover, observing the waveform in Fig. 9(d) it can be concluded that a very high value of damping will impede interwell vibration. Still, it can be observed that the performance of the panel for c=0.15kg/sec is much ameliorated compared to the reference design, concluding that even for a non-optimal damping value (lower or higher than the optimal range) the NSN oscillators can absorb a large amount of structural vibration close to resonances.

3.4. Parametric study on the performance of the structural system with respect to the amplitude of vibration

The dynamics of the NSN is expected to display three different types of behaviours with increasing basis oscillation amplitude. In the low amplitude range intrawell oscillations are expected as observed in Figs. 4b and 8a. In the medium amplitude range, interwell chaotic oscillations are expected, while for very large amplitudes the negative stiffness and the two wells do not have a substantial effect on the global dynamics anymore as observed in Fig. 4c.

In order to further understand the performance of the implemented set of oscillators the response is investigated vis-à-vis the structural vibration level. For this purpose and excitation amplitude is imposed at $x = 0.18$m, $y = 0.12$m in order to evaluate the induced additional damping. The frequency response at the first resonance of the master structure, as well as typical oscillatory waveforms are presented in Fig. 10. The oscillator has m_{res}=0.004kg, h=0.015m, c=0.05kg/sec, q_0=0.001, L=0.021m, EI=4×10^{-6}GPam^4 for all cases. As discussed in Sec.2.3, increase of vibration amplitude is expected to push m_{osc} into interwell vibration facilitating energy absorption. On the other hand, there is a maximum amount of energy that can be damped by the mechanism, therefore when structural energy increases the dissipated energy ratio η is inevitably expected to decrease.

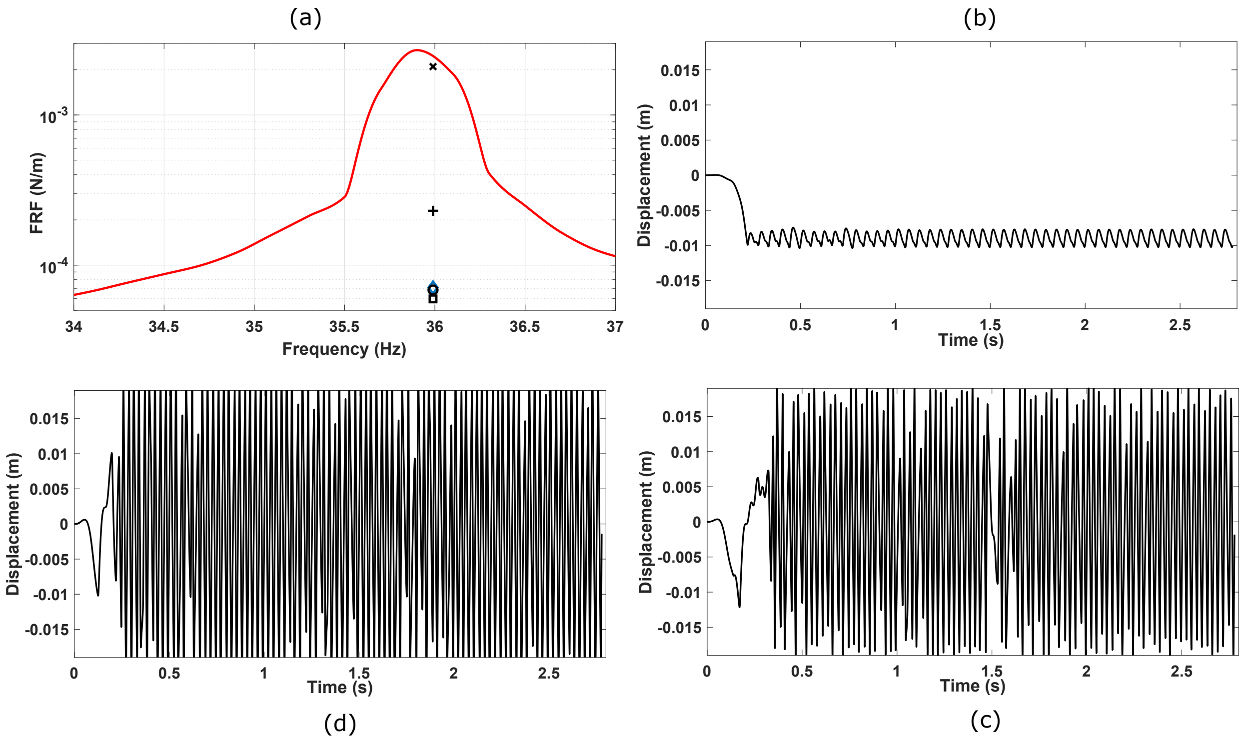

Figure 10: Parametric study of the structural response at the first natural frequency of the sandwich panel with respect to structural vibration amplitude A_{exc} imposed at $x = 0.18$m, $y = 0.12$m: (a) The response in the frequency domain shown at 36Hz for A_{exc}=0.3mm (x), A_{exc}=3mm (□), A_{exc}=5mm (o), A_{exc}=7mm (◇), A_{exc}=15mm (+). (b) Typical transient waveform for m_{osc} when A_{exc}=0.3mm, (c) Typical transient waveform for m_{osc} when A_{exc}=5mm, (d) Typical transient waveform for m_{osc} when A_{exc}=15mm.

The response of the panel shown in Fig. 10(a) demonstrates some important trends related to the excitation amplitude. Unsurprisingly, a very low excitation amplitude (see Fig. 10(b)) impedes m_{osc} from entering an interwell vibration mode therefore resulting in poor damping performance. On the other hand, imposing a very high excitation amplitude close to the thickness of the panel (see Fig. 10(d)) helps m_{osc} to go into interwell vibration with a large amplitude, however simultaneously reduced the portion of structural energy damped by the oscillators and results once again in non-optimal performance. Excitation amplitudes in the range A_{exc}=3-7mm seem to be most beneficial for maximising the effects of the NSN oscillators.

It can be concluded that in Fig. 10 the three expected ranges of oscillations are observed accompanied with the corresponding anticipated impact on the dissipation level. In the low amplitude range the response is generally similar to Fig. 10(b) with oscillators mainly moving in an intrawell mode. Minimum impact on the global response levels of the structure should be expected in that range. In the medium amplitude range, interwell chaotic oscillations are expected with the time domain signatures resembling Fig. 10(c). This is the range where maximum impact on the dissipated energy ratio should be expected since the dissipated energy is closer to the vibrational energy of the master structure. For very large basis amplitudes, signatures resemble Fig. 10(d). The oscillation amplitude for m_{osc} increases slightly, however its impact on the dissipated energy ratio diminishes given the increase of the vibrational energy stored in the master structure.

It should be noted that the above observations also provide insight on why the beneficial effects of the oscillators only become apparent close to the master structure's resonances (see Fig. 7). It is close to these resonances that a concentrated forcing or amplitude can induce high levels of vibration over the entire surface of the panel. This high level of vibration activates a maximum number of oscillators (obviously oscillators laying close to vibration nodes with no motion are still not activated). In contrast to what happens close to resonances, away from them a concentrated forcing or amplitude cannot efficiently spread over the entire surface of the structure, implying a minimum amount of resonators being activated.

3.5. Discussion on the broadband beneficial effects and on the dissipated energy ratio

In order to further investigate the advantages and limitations of the NSN oscillators additional computations are hereby performed. The fist seven out-of-plane (all of flexural nature) global resonances of the panel are taking place at 36Hz, 75Hz, 90Hz, 142Hz, 145Hz, 192Hz and 206Hz. The broadband nature of the beneficial effects is initially explored, expanding the frequency range of the calculations. The results are presented in Fig. 11 for the oscillator design used throughout this manuscript (m_{res}=0.004kg, h=0.015m, c=0.05kg/sec, q_0=0.001, L=0.021m, EI=4×10^{-6}GPam^4) and for A_{exc}=3mm at at $x = 0.18$m, $y = 0.12$m. Steady-state sinusoidal excitations are imposed and the response is measured at frequencies close to structural resonances.

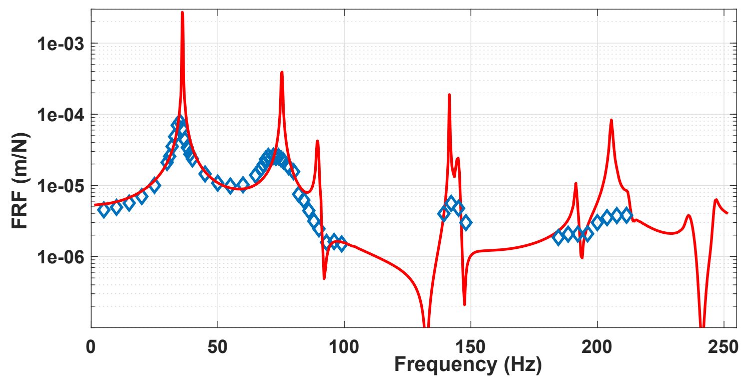

Figure 11: Structural response at x=0.54m, y=0.12m. Comparison between the NSN design ⋄ and the linear design with oscillators tuned higher than 300Hz.

It is demonstrated that the first six flexural resonances are successfully dissipated all the way up to 250Hz. At this point it should be stressed that inducing this type of broadband dissipation with linear resonators would demand at least six different designs of resonators implemented within the panel. Spatial optimisation of the distribution of these resonators would by itself be a complex problem to solve. Moreover, having only one sixth of the resonators tuned at a specific frequency would weaken the damping effect of the linear design and results would look very different than the ones presented in Fig. 7 for a periodic structure. On the downside, it should be noted that having high vibration amplitudes (A_{exc}=3mm imposed for Fig. 7) above the first one or two natural frequencies is not always the case in mechanical applications. Having a much lower vibration amplitude as demonstrated in Fig. 10 can result in low power absorption by the NSN design.

The dissipated energy ratio η is computed and presented in Fig. 12. It is reminded that this is defined as $\eta = E_{diss}/E_{struc}$ with the E_{struc} being computed as twice the sum of kinetic energies over the nodes of the master structure and E_{diss} being the energy absorbed by the viscous element during one cycle. The presented values are averaged over ten cycles.

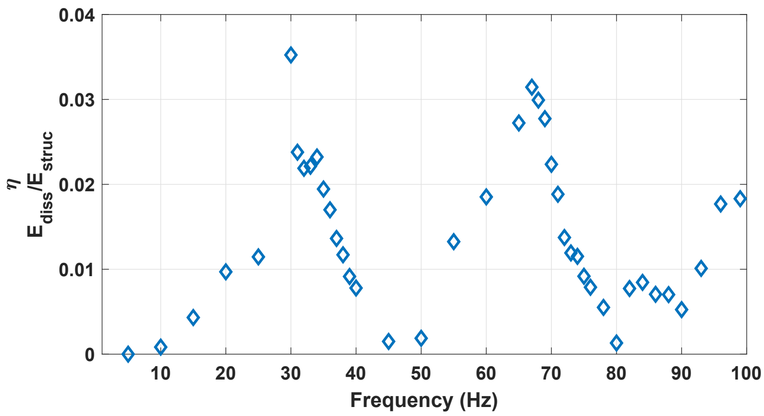

Figure 12: The dissipated energy ratio calculated from 5Hz to 100 Hz for the design presented in Fig. 7.

It is evident that η increases close to structural resonances. Indeed, close to resonances the flexural mode shapes of the panel are activated and a concentrated forcing or amplitude can induce high levels of vibration over the entire surface of the panel, thus activating a maximum number of oscillators and inducing high levels of effective damping as also demonstrated in Fig. 7.

4. Critical outlook on design optimization, manufacturing aspects and necessary future developments

The NSN design has exhibited promising capabilities for providing tunable and broadband vibration isolation. A sophisticated design optimization exercise is the natural next step to explore the full potential of the proposed approach. The optimization should include the effects on NSN performance by varying the key design parameters, such as NSN mass, dimensions and material properties. It is important to establish a thorough understanding as to why the NSN is acting as an energy absorbing mechanism in a rather broadband sense by exploring the vibration modes near resonance between the primary system and the NSN. Key questions to answer are (i) How does the energy input affect the NSN activation in the above vibration modes and (ii) How does the NSN damping influences its ability to absorb vibration energy. Stability characterisation of the system equilibria and basins of attraction would be useful tools to map the expected behaviour of the system. Considering that NSN oscillators are classically employed as a tool for absorbing vibration energy at very low amplitudes and frequencies, the proposed work attempts to shift this standard regard towards negative stiffness systems and expand their application towards higher frequency ranges and distributed vibrating structural ensembles. The optimum number and distribution strategy of the NSNs on the primary structure should be investigated, as well as the maximum NSN vibration amplitude permittable by the geometric constraints as additional design criteria. Experimental validation is also the major focus of the following work, given it is hard to fabricate such structures by traditional conventional manufacturing methods, additive manufacturing technologies, which are widely used for the metamaterial and sandwich structure fabrication [7, 81–83],, are planned to manufacture the sandwich structures and nonlinear mechanisms.

5. Concluding remarks

This paper investigated the vibration absorption performance of continuous multilayered structures incorporating NSN oscillators. The NSN oscillators were composed of a small damped mass supported by two buckled beams which were hinged at the ends. The dynamic responses of a single NSN oscillator mounted in a vibrating unit were first analyzed by an analytical model to explore designs that are able to perform interwell oscillation. The NSN oscillators were subsequently implemented in a vibrating multilayered sandwich structure for energy absorption. The structural responses of composite sandwich structures were estimated by FE methods with NSN oscillators simulated by nonlinear spring-mass dampers. An equivalent linear system consisting of the same master structure and linear oscillators was also simulated for comparison. It was found that the sandwich structures with NSN oscillators exhibited broader vibration absorption. When the excitation is of broadband nature and of high amplitude then the suggested NSN oscillators outperform their equivalent linear counterparts. As a contrast, structures with linear resonators have strong vibration suppression within narrow tuned stopbands. If the excitation frequency is narrow and deterministically defined then a linear resonant structure would outperform the presented system comprising NSN oscillators. This paper provides a numerical proof of concept for structures incorporating NSN oscillators, which show great potential to construct tunable broadband vibration absorption configurations. Optimization, experimental validation and durability and reliability assessments are the major next steps for the proposed NSN design.

6. Acknowledgements

This work was supported by the H2020 Marie Sklodowska-Curie grant [grant number DiaMoND 785859].

References

1. Liu, Z., Zhang, X., Mao, Y., Zhu, Y., Yang, Z., Chan, C.T., Sheng, P.. Locally resonant sonic materials. *science* 2000;289(5485):1734–1736.
2. Zhang, H., Xiao, Y., Wen, J., Yu, D., Wen, X.. Flexural wave band gaps in metamaterial beams with membrane-type resonators: theory and experiment. *Journal of Physics D: Applied Physics* 2015;48(43):435305.
3. Huang, T.Y., Shen, C., Jing, Y.. Membrane-and plate-type acoustic metamaterials. *The Journal of the Acoustical Society of America* 2016;139(6):3240–3250.
4. Langfeldt, F., Kemsies, H., Gleine, W., Von Estorff, O.. Perforated membrane-type acoustic metamaterials. *Physics Letters A* 2017;381(16):1457–1462.
5. Chen, J., Sharma, B., Sun, C.. Dynamic behaviour of sandwich structure containing spring-mass resonators. *Composite Structures* 2011;93(8):2120–2125.
6. Peng, H., Pai, P.F.. Acoustic metamaterial plates for elastic wave absorption and structural vibration suppression. *International Journal of Mechanical Sciences* 2014;89:350–361.
7. Meng, H., Chronopoulos, D., Fabro, A., Elmadih, W., Maskery, I.. Rainbow metamaterials for broadband multi-frequency vibration attenuation: Numerical analysis and experimental validation. *Journal of Sound and Vibration* 2020;465:115005.
8. Meng, H., Chronopoulos, D., Fabro, A.T., Maskery, I., Chen, Y.. Optimal design of rainbow elastic metamaterials. *International Journal of Mechanical Sciences* 2020;165:105185.
9. Fabro, A.T., Meng, H., Chronopoulos, D.. Uncertainties in the attenuation performance of a multi-frequency metastructure from additive manufacturing. *Mechanical Systems and Signal Processing* 2020;138:106557.
10. Meng, H., Chronopoulos, D., Fabro, A.T.. Numerical simulation data for the dynamic properties of rainbow metamaterials. *Data in Brief* 2020;.
11. Barnhart, M.V., Xu, X., Chen, Y., Zhang, S., Song, J., Huang, G.. Experimental demonstration of a dissipative multi-resonator metamaterial for broadband elastic wave attenuation. *Journal of Sound and Vibration* 2019;438:1–12.
12. Peng, H., Pai, P.F., Deng, H.. Acoustic multi-stopband metamaterial plates design for broadband elastic wave absorption and vibration suppression. *International Journal of Mechanical Sciences* 2015;103:104–114.
13. Pai, P.F., Peng, H., Jiang, S.. Acoustic metamaterial beams based on multi-frequency vibration absorbers. *International Journal of Mechanical Sciences* 2014;79:195–205.

14. Xiao, Y., Wen, J., Wen, X.. Broadband locally resonant beams containing multiple periodic arrays of attached resonators. *Physics Letters A* 2012;376(16):1384–1390.
15. Xiao, Y., Wen, J., Yu, D., Wen, X.. Flexural wave propagation in beams with periodically attached vibration absorbers: band-gap behavior and band formation mechanisms. *Journal of Sound and Vibration* 2013;332(4):867–893.
16. Li, Y., Zhu, L., Chen, T.. Plate-type elastic metamaterials for low-frequency broadband elastic wave attenuation. *Ultrasonics* 2017;73:34–42.
17. Carrella, A., Brennan, M., Waters, T.. Static analysis of a passive vibration isolator with quasi-zero-stiffness characteristic. *Journal of sound and vibration* 2007;301(3-5):678–689.
18. Carrella, A., Brennan, M., Kovacic, I., Waters, T.. On the force transmissibility of a vibration isolator with quasi-zero-stiffness. *Journal of Sound and Vibration* 2009;322(4-5):707–717.
19. Kovacic, I., Brennan, M.J., Waters, T.P.. A study of a nonlinear vibration isolator with a quasi-zero stiffness characteristic. *Journal of sound and vibration* 2008;315(3):700–711.
20. Tang, B., Brennan, M.. On the shock performance of a nonlinear vibration isolator with high-static-low-dynamic-stiffness. *International Journal of Mechanical Sciences* 2014;81:207–214.
21. Liu, F., Theodossiades, S., McFarland, D., Vakakis, A.F., Bergman, L.. Tailoring strongly nonlinear negative stiffness. *Journal of Mechanical Design* 2014;136(2).
22. Hao, Z., Cao, Q.. The isolation characteristics of an archetypal dynamical model with stable-quasi-zero-stiffness. *Journal of sound and vibration* 2015;340:61–79.
23. Yao, Y., Li, H., Li, Y., Wang, X.. Analytical and experimental investigation of a high-static-low-dynamic stiffness isolator with cam-roller-spring mechanism. *International Journal of Mechanical Sciences* 2020;186:105888.
24. Zhou, J., Wang, X., Xu, D., Bishop, S.. Nonlinear dynamic characteristics of a quasi-zero stiffness vibration isolator with cam–roller–spring mechanisms. *Journal of Sound and Vibration* 2015;346:53–69.
25. Wang, X., Zhou, J., Xu, D., Ouyang, H., Duan, Y.. Force transmissibility of a two-stage vibration isolation system with quasi-zero stiffness. *Nonlinear Dynamics* 2017;87(1):633–646.
26. Zhang, W., Zhao, J.. Analysis on nonlinear stiffness and vibration isolation performance of scissor-like structure with full types. *Nonlinear Dynamics* 2016;86(1):17–36.
27. Sun, X., Jing, X.. Analysis and design of a nonlinear stiffness and damping system with a scissor-like structure. *Mechanical Systems and Signal Processing* 2016;66:723–742.
28. Sun, X., Jing, X., Xu, J., Cheng, L.. Vibration isolation via a scissor-like structured platform. *Journal of Sound and Vibration* 2014;333(9):2404–2420.
29. Wu, Z., Jing, X., Bian, J., Li, F., Allen, R.. Vibration isolation by exploring bio-inspired structural nonlinearity. *Bioinspiration & biomimetics* 2015;10(5):056015.
30. Dai, H., Jing, X., Wang, Y., Yue, X., Yuan, J.. Post-capture vibration suppression of spacecraft via a bio-inspired isolation system. *Mechanical Systems and Signal Processing* 2018;105:214–240.
31. Bian, J., Jing, X.. Superior nonlinear passive damping characteristics of the bio-inspired limb-like or x-shaped structure. *Mechanical Systems and Signal Processing* 2019;125:21–51.
32. Platus, D.L.. Negative-stiffness-mechanism vibration isolation systems. In: *Optomechanical Engineering and Vibration Control*; vol. 3786. International Society for Optics and Photonics; 1999:98–105.
33. Yang, J., Xiong, Y., Xing, J.. Dynamics and power flow behaviour of a nonlinear vibration isolation system with a negative stiffness mechanism. *Journal of sound and vibration* 2013;332(1):167–183.
34. Wang, X., Liu, H., Chen, Y., Gao, P.. Beneficial stiffness design of a high-static-low-dynamic-stiffness vibration isolator based on static and dynamic analysis. *International Journal of Mechanical Sciences* 2018;142:235–244.
35. Zhang, J., Li, D., Chen, M.J., Dong, S.. An ultra-low frequency parallel connection nonlinear isolator for precision instruments. In: *Key Engineering Materials*; vol. 257. Trans Tech Publ; 2004:231–238.
36. Le, T.D., Ahn, K.K.. A vibration isolation system in low frequency excitation region using negative stiffness structure for vehicle seat. *Journal of Sound and Vibration* 2011;330(26):6311–6335.
37. Fulcher, B.A., Shahan, D.W., Haberman, M.R., Conner Seepersad, C., Wilson, P.S.. Analytical and experimental investigation of buckled beams as negative stiffness elements for passive vibration

and shock isolation systems. *Journal of Vibration and Acoustics* 2014;136(3).
38. Kashdan, L., Seepersad, C., Haberman, M., Wilson, P.S.. Design, fabrication and evaluation of negative stiffness elements. In: *Proceedings of the 20th Annual International Solid Freeform Fabrication Symposium*. 2009:.
39. Haberman, M.R.. Design of high loss viscoelastic composites through micromechanical modeling and decision based materials design. Ph.D. thesis; Georgia Institute of Technology; 2007.
40. Virgin, L., Davis, R.. Vibration isolation using buckled struts. *Journal of Sound and Vibration* 2003;260(5):965–973.
41. Lee, C.M., Goverdovskiy, V., Temnikov, A.. Design of springs with "negative" stiffness to improve vehicle driver vibration isolation. *Journal of sound and vibration* 2007;302(4-5):865–874.
42. Woodard, S.E., Housner, J.M.. Nonlinear behavior of a passive zero-spring-rate suspension system. *Journal of Guidance, Control, and Dynamics* 1991;14(1):84–89.
43. Liu, X., Huang, X., Hua, H.. On the characteristics of a quasi-zero stiffness isolator using euler buckled beam as negative stiffness corrector. *Journal of Sound and Vibration* 2013;332(14):3359–3376.
44. Huang, X., Liu, X., Sun, J., Zhang, Z., Hua, H.. Effect of the system imperfections on the dynamic response of a high-static-low-dynamic stiffness vibration isolator. *Nonlinear Dynamics* 2014;76(2):1157–1167.
45. Huang, X., Liu, X., Sun, J., Zhang, Z., Hua, H.. Vibration isolation characteristics of a nonlinear isolator using euler buckled beam as negative stiffness corrector: a theoretical and experimental study. *Journal of Sound and Vibration* 2014;333(4):1132–1148.
46. Xu, D., Yu, Q., Zhou, J., Bishop, S.. Theoretical and experimental analyses of a nonlinear magnetic vibration isolator with quasi-zero-stiffness characteristic. *Journal of Sound and Vibration* 2013;332(14):3377–3389.
47. Zheng, Y., Zhang, X., Luo, Y., Yan, B., Ma, C.. Design and experiment of a high-static–low-dynamic stiffness isolator using a negative stiffness magnetic spring. *Journal of Sound and Vibration* 2016;360:31–52.
48. Wu, W., Chen, X., Shan, Y.. Analysis and experiment of a vibration isolator using a novel magnetic spring with negative stiffness. *Journal of Sound and Vibration* 2014;333(13):2958–2970.
49. Robertson, W.S., Kidner, M., Cazzolato, B.S., Zander, A.C.. Theoretical design parameters for a quasi-zero stiffness magnetic spring for vibration isolation. *Journal of Sound and Vibration* 2009;326(1-2):88–103.
50. Carrella, A., Brennan, M., Waters, T., Shin, K.. On the design of a high-static–low-dynamic stiffness isolator using linear mechanical springs and magnets. *Journal of Sound and Vibration* 2008;315(3):712–720.
51. Dong, G., Zhang, X., Xie, S., Yan, B., Luo, Y.. Simulated and experimental studies on a high-static-low-dynamic stiffness isolator using magnetic negative stiffness spring. *Mechanical Systems and Signal Processing* 2017;86:188–203.
52. Benacchio, S., Malher, A., Boisson, J., Touzé, C.. Design of a magnetic vibration absorber with tunable stiffnesses. *Nonlinear Dynamics* 2016;85(2):893–911.
53. Zhou, N., Liu, K.. A tunable high-static–low-dynamic stiffness vibration isolator. *Journal of Sound and Vibration* 2010;329(9):1254–1273.
54. Zhou, N., Liu, K.. Characterization of an electromagnetic vibration isolator. *Journal of Electromagnetic Analysis and Applications* 2011;2011.
55. Pu, H., Yuan, S., Peng, Y., Meng, K., Zhao, J., Xie, R., Huang, Y., Sun, Y., Yang, Y., Xie, S., et al. Multi-layer electromagnetic spring with tunable negative stiffness for semi-active vibration isolation. *Mechanical Systems and Signal Processing* 2019;121:942–960.
56. Romeo, F., Sigalov, G., Bergman, L.A., Vakakis, A.F.. Dynamics of a linear oscillator coupled to a bistable light attachment: numerical study. *Journal of Computational and Nonlinear Dynamics* 2015;10(1).
57. Habib, G., Romeo, F.. The tuned bistable nonlinear energy sink. *Nonlinear Dynamics* 2017;89(1):179–196.

58. Romeo, F., Manevitch, L., Bergman, L., Vakakis, A.. Transient and chaotic low-energy transfers in a system with bistable nonlinearity. *Chaos: An Interdisciplinary Journal of Nonlinear Science* 2015;25(5):053109.
59. Al-Shudeifat, M.A.. Highly efficient nonlinear energy sink. *Nonlinear Dynamics* 2014;76(4):1905–1920.
60. Zhou, J., Wang, K., Xu, D., Ouyang, H.. Multi-low-frequency flexural wave attenuation in euler–bernoulli beams using local resonators containing negative-stiffness mechanisms. *Physics Letters A* 2017;381(37):3141–3148.
61. Zhou, J., Wang, K., Xu, D., Ouyang, H.. Local resonator with high-static-low-dynamic stiffness for lowering band gaps of flexural wave in beams. *Journal of Applied Physics* 2017;121(4):044902.
62. Zhou, J., Dou, L., Wang, K., Xu, D., Ouyang, H.. A nonlinear resonator with inertial amplification for very low-frequency flexural wave attenuations in beams. *Nonlinear Dynamics* 2019;96(1):647–665.
63. Casalotti, A., El-Borgi, S., Lacarbonara, W.. Metamaterial beam with embedded nonlinear vibration absorbers. *International Journal of Non-Linear Mechanics* 2018;98:32–42.
64. Wang, K., Zhou, J., Cai, C., Xu, D., Ouyang, H.. Mathematical modeling and analysis of a meta-plate for very low-frequency band gap. *Applied Mathematical Modelling* 2019;73:581–597.
65. Wang, K., Zhou, J., Wang, Q., Ouyang, H., Xu, D.. Low-frequency band gaps in a metamaterial rod by negative-stiffness mechanisms: Design and experimental validation. *Applied Physics Letters* 2019;114(25):251902.
66. Kani, M., Khadem, S., Pashaei, M., Dardel, M.. Vibration control of a nonlinear beam with a nonlinear energy sink. *Nonlinear Dynamics* 2016;83(1-2):1–22.
67. Carrella, A., Brennan, M., Waters, T., Lopes Jr, V.. Force and displacement transmissibility of a nonlinear isolator with high-static-low-dynamic-stiffness. *International Journal of Mechanical Sciences* 2012;55(1):22–29.
68. Milovanovic, Z., Kovacic, I., Brennan, M.J.. On the displacement transmissibility of a base excited viscously damped nonlinear vibration isolator. *Journal of Vibration and Acoustics* 2009;131(5).
69. Bažant, Z., Cedolin, L.. Stability of Structures. Oxford University Press: New York, Oxford (1991). 1991.
70. Peng, Z., Meng, G., Lang, Z., Zhang, W., Chu, F.. Study of the effects of cubic nonlinear damping on vibration isolations using harmonic balance method. *International Journal of Non-Linear Mechanics* 2012;47(10):1073–1080.
71. Korn, G.A., Korn, T.M.. Mathematical handbook for scientists and engineers: definitions, theorems, and formulas for reference and review. Courier Corporation; 2000.
72. Kovacic, I., Brennan, M.J., Lineton, B.. On the resonance response of an asymmetric duffing oscillator. *International Journal of Non-Linear Mechanics* 2008;43(9):858–867.
73. Nayfeh, A.H., Mook, D.T.. Nonlinear oscillations. John Wiley & Sons; 2008.
74. Hunt, K.H., Crossley, F.R.E.. Coefficient of restitution interpreted as damping in vibroimpact. 1975.
75. Nucera, F., Vakakis, A.F., McFarland, D., Bergman, L., Kerschen, G.. Targeted energy transfers in vibro-impact oscillators for seismic mitigation. *Nonlinear Dynamics* 2007;50(3):651–677.
76. Wagg, D.. A note on coefficient of restitution models including the effects of impact induced vibration. *Journal of Sound and Vibration* 2007;300(3-5):1071–1078.
77. Claeys, C., de Melo Filho, N.G.R., Van Belle, L., Deckers, E., Desmet, W.. Design and validation of metamaterials for multiple structural stop bands in waveguides. *Extreme Mechanics Letters* 2017;12:7–22.
78. Elmadih, W., Chronopoulos, D., Syam, W., Maskery, I., Meng, H., Leach, R.. Three-dimensional resonating metamaterials for low-frequency vibration attenuation. *Scientific reports* 2019;9(1):1–8.
79. Parseh, M., Dardel, M., Ghasemi, M.H.. Performance comparison of nonlinear energy sink and linear tuned mass damper in steady-state dynamics of a linear beam. *Nonlinear Dynamics* 2015;81(4):1981–2002.
80. Sun, L., Au-Yeung, K.Y., Yang, M., Tang, S.T., Yang, Z., Sheng, P.. Membrane-type resonator as an effective miniaturized tuned vibration mass damper. *AIP Advances* 2016;6(8):085212.
81. Meng, H., Galland, M.A., Ichchou, M., Bareille, O., Xin, F., Lu, T.. Small perforations in

corrugated sandwich panel significantly enhance low frequency sound absorption and transmission loss. *Composite Structures* 2017;182:1–11.
82. Zaharia, S.M., Enescu, L.A., Pop, M.A.. Mechanical performances of lightweight sandwich structures produced by material extrusion-based additive manufacturing. *Polymers* 2020;12(8):1740.
83. Lu, C., Qi, M., Islam, S., Chen, P., Gao, S., Xu, Y., Yang, X.. Mechanical performance of 3d-printing plastic honeycomb sandwich structure. *International Journal of Precision Engineering and Manufacturing-Green Technology* 2018;5(1):47–54.